A Steerable, Untethered, 250 $\times$ 60 μm MEMS Mobile Micro-Robot

Bruce R. Donald[1,2,*] , Christopher G. Levey[3] , Craig D. McGray[1] , Igor Paprotny[1], and Daniela Rus[4]

[1] Dartmouth Computer Science Department, Hanover, NH 03755
[2] Dartmouth Chemistry Department, Hanover, NH 03755
[3] Dartmouth Thayer School of Engineering, Hanover, NH 03755
[4] Department of Electrical Engineering and Computer Science, Massachusetts Institute of Technology, Boston, MA

Abstract. We present a steerable, electrostatic, untethered, MEMS micro-robot, with dimensions of 60 μm by 250 μm by 10 μm. This micro-robot is **1 to 2 orders of magnitude** smaller in size than previous micro-robotic systems. The device consists of a curved, cantilevered steering arm, mounted on an untethered scratch drive actuator. These two components are fabricated monolithically from the same sheet of conductive polysilicon, and receive a common power and control signal through a capacitive coupling with an underlying electrical grid. All locations on the grid receive the same power and control signal, so that the devices can be operated without knowledge of their position on the substrate and without constraining rails or tethers. Control and power delivery waveforms are broadcast to the device through the capacitive power coupling, and are decoded by the electromechanical response of the device body. Individual control of the component actuators provides two distinct motion gaits (forward motion and turning), which together allow full coverage of a planar workspace (the robot is globally controllable). These MEMS micro-robots demonstrate turning error of less than $3.7^\circ/\mathrm{mm}$ during forward motion, turn with radii as small as 176 μm, and achieve speeds of over 200 μm/sec, with an average step size of 12 nm. They have been shown to operate open-loop for distances exceeding 35 cm without failure, and can be controlled through teleoperation to navigate complex paths.

1 Introduction

This paper addresses the design, fabrication, and control of micro-robots that are small enough to locomote on the surface of an integrated circuit, and to interact with parts as small as individual MEMS components. While there are many MEMS devices with sizes measured in tens of microns, the smallest micro-robotic systems yet produced have dimensions on the order of millimeters or centimeters. A primary reason for this, is that existing micro-robot architectures employ a rigid chassis on which to mount power, locomotion, steering, communication, and control systems. While these active components often include thin-film MEMS actuators, the chassis is a macro-scale part such as, for example, a silicon die. For this reason, these micro-robots are often referred to as "walking chips" [1–5].

* Corresponding author (e-mail: brd@cs.dartmouth.edu)

We build on our previous work [6,7], which describes MEMS untethered scratch drive actuators that can move only along *straight-line* (linear) trajectories, and demonstrate a new generation of micro-robots that are *steerable along arbitrary trajectories* (i.e., globally controllable [8] in $\mathbb{R}^2 \times S^1$). Our new devices integrate, in a single thin film device body, not only power delivery, locomotion, and communications, but now also steering and control systems. This allows us to build a micro-robot that is one to two orders of magnitude smaller in length than previous systems, and many thousands of times smaller in overall mass. The device is capable of two distinct motions: it can either translate forwards, or turn through an arc with a fixed minimum radius of approximately 175 μm. Alternation of these two motion primitives allows for execution of turns with any arbitrary radius larger than the minimum. These two operations are sufficient to provide our device with global controllability.

Figure 1 shows the structure of this device. It consists of an untethered scratch drive actuator [6,7] (**A**), with a cantilevered steering arm (**B**) that protrudes from one side.

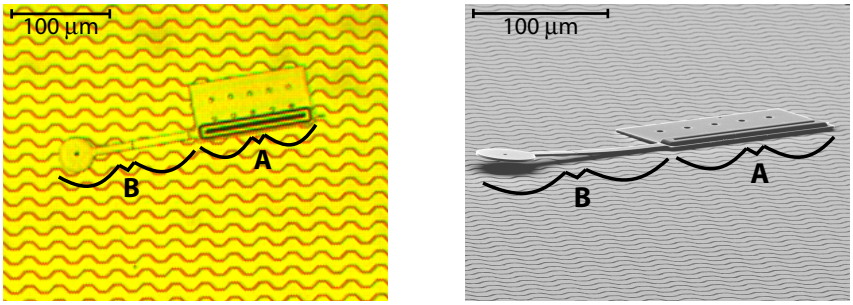

Fig. 1. Optical (**left**) and electron (**right**) micrographs of an electrostatic micro-robot. The device consists of an untethered scratch drive actuator (**A**) [6,7], with a cantilevered steering arm (**B**) that protrudes from one side. The untethered scratch drive is used for propulsion, while the steering arm can be raised or lowered to turn. An array of insulated interdigitated electrodes (lighter-colored background) provides electrical power and control signals to the device.

The untethered scratch drive is used for locomotion, while the steering arm is used to raise or lower a stylus into contact with the substrate. When this stylus is in contact with the substrate, it provides enough friction to cause the device as a whole to turn. The device receives its electrical power and control signals through a grid of insulated interdigitated electrodes that cover the device's operating environment. Since the control signal and electrical power are both available to a device anywhere within this environment, the device can move freely, unconstrained by wires or rails that power most electrostatic MEMS devices. The operating environment used for the devices presented in this paper extends across 6.25 square millimeters of surface, and could be made even larger if desired.

Previous approaches to micro-robot control rely on providing signals to all subsystems continuously and simultaneously. In macro-scale robotic systems, instructions are generally only transmitted once, and are then stored on-board the device until they are replaced with a new instruction. While macro-scale devices typically implement this data storage with electronics, a thin-film MEMS device can utilize the simpler alternative approach of storing state information in the electromechanical flexure of the active components. The devices described in the present paper are controlled through *electromechanical state-based* component addressing. We exploit the hysteresis of the components by applying sequences of voltages in a control waveform. First, the desired behavior (forward motion or turning) is specified by an electrical pulse, and is stored in the elastic flexure of the device steering arm. Then, a continuous AC drive waveform is applied to actuate the scratch drive and produce motion. This is achieved by nesting the electromechanical hysteresis loops of the scratch drive within the hysteresis loop of the actuator steering arm.

The micro-robots are composed of polycrystalline silicon using a multi-user foundry MEMS process [9]. After receipt from the foundry, the die are coated with 830 Å of thermally evaporated chromium to create a well-controlled stress gradient in the cantilevered steering arms, determining the cantilevers' tip deflection. Full details of the fabrication process are presented in Appendix A.

The performance of the devices was tested under both open-loop and teleoperated control. Micro-probes connect the electrodes to a function generator and amplifier. During teleoperation, a human operator switches between two different waveforms produced by the function generator in order to control the motion of the untethered micro-robotic device (see Figure 1). A camera records the device's motion through an optical microscope, allowing the operator to make the necessary adjustment to guide the device along the desired path. Section 6 discusses the reliability of the basic motion primitives, and shows some examples of more complex paths produced through teleoperation. The device has the ability to push and manipulate other MEMS-scale components [6,7].

The introduction of a micro-robotic device with size less than 250 μm could extend and enable the set of micro-robot applications that have been previously identified. These include security and surveillance [3]; exploration of hazardous environments; and biomedical research [10]. Of particular interest are those applications which allow a controlled environment for micro-robot operation, in which cleanliness and surface smoothness can be carefully maintained, and in which an ambient power source can be conveniently applied. Such applications include the manipulation and assembly of hybrid microsystems [10,3]; micro-scale self-reconfiguring robotics [11]; and MEMS infosecurity self-assembly [12], where autonomous locomotion of micro-devices is a primary requirement. We envision that the devices, designs, and control systems presented in this paper will enable these applications for micro-robots.

2 Related Work

Previous work has produced a number of micro-robots with dimensions on the order of millimeters or centimeters [1,13,3,5]. Past systems have delivered power

through vibration [14], photo-thermal transduction [1], inductive coupling [2], and electrically through gold bonding wire [3]. The capacitively-coupled electrostatic power delivery mechanism that we described in [6,7] is well-suited to the untethered devices presented in the current paper. While the linear untethered scratch drive actuators presented in [6,7] provide some building blocks for our current power delivery system, the devices in [6,7] could only be driven in straight lines. The present paper describes the design, fabrication, and control challenges in making *untethered steerable micro-robots* that can execute complex paths and are globally controllable [8]. These capabilities are essential for micro-robotic applications.

In previous micro-robotic devices, steering systems have been implemented primarily through differential operation of matched pairs or arrays of actuators [1,14]. In these devices, each actuator contributes a small propulsive force to the device as a whole, which then moves as the vector sum of the forces provided by the component actuators. The device described in the present paper uses only two actuators: one for propulsion, and a second one to raise and lower a stylus into frictional contact with the substrate. This simplifies the overall device, reduces its size, and allows for precisely-controlled turning motions, even in the presence of small surface abnormalities.

3 Power Delivery

In [6,7], we presented a mechanism for delivering power to linear untethered MEMS actuators, via a capacitive coupling across a thin film of thermal silica. In this mechanism, a silicon substrate is covered with rows of insulated interdigitated electrodes. When a conductive actuator, such as a scratch drive, rests on top of these electrodes (as shown on Figure 1), it forms the capacitive circuit with the underlying electrodes. In this way, a voltage is applied to the actuator, regardless of its position and orientation relative to the underlying electrodes (i.e. no position-restricting wires or tethers are required.) Each time the voltage is cycled, the scratch drive moves forward by a small increment, known as the *step size*. The frequency at which this cycle occurs is known as the *stepping frequency*, and the speed of the actuator is the product of its stepping frequency and its average step size. To deliver power to our steerable MEMS micro-robots, we have used substrates covered with zirconia-insulated gold electrodes. The edges of the electrodes are jagged (as shown in Figure 1) to help maintain a consistent voltage on the actuator, regardless of the actuator's pose. Further details regarding the power delivery mechanism are provided in Appendix B.

4 Steering

The micro-robot controls its direction by raising and lowering its steering arm. Figure 2 shows a close-up view of this actuator. It consists of a 133-μm-long curved cantilever beam, with a disc at its tip. At the center of the disc, a 0.75-μm-high dimple serves as the stylus for frictional contact. The dimple has a radius of 1.5 μm, and the surrounding disc has a radius of 18 μm.

When the steering arm is in the raised position, the device as a whole behaves like a linear untethered scratch drive actuator [6,7]. In this case, when an oscillating

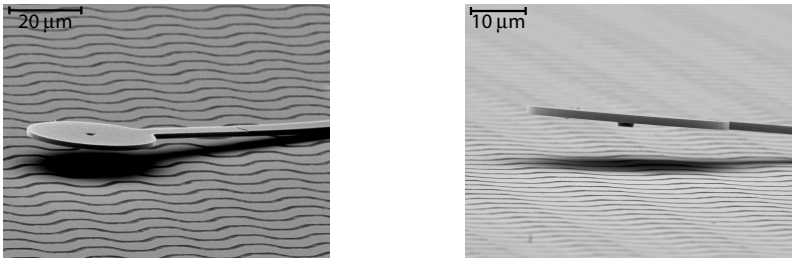

Fig. 2. Electron micrographs of the steering arm sub-system. The stylus used for frictional contact consists of a 0.75-μm dimple, visible beneath the end of the arm. An 18-μm-radius disc increases the electrostatic force on the arm, which is curled upwards to increase the gap between the stylus and the substrate.

voltage is applied, the device will move forward in a straight line. To actuate the device forward, we chose a pulsed waveform with peak and minimum electrode-to-electrode voltages of 112 V and 39 V, respectively.

Note that the voltage applied to the electrode array differs from the potential between the scratch-drive actuator and the substrate, due to the nature of the power delivery mechanism. The power delivery mechanism forms a capacitive circuit between the electrodes and the scratch drive actuator (see Figure 8, p. 15, Appendix B). This circuit sets the potential of the scratch-drive actuator plate to approximately the midpoint between the potential of the inter-digitated electrodes. Since the "even" electrodes (see Figure 8) are held at 0 V while the pulsed drive waveform is only applied to the "odd" electrodes (Figure 8), the resulting voltage affecting the scratch-drive actuator is approximately half of the voltage applied to the electrode field. Thus, the potential affecting the scratch-drive actuator during the application of the power delivery waveform has an effective peak and minimum voltages of approximately 56 V and 19 V, respectively.

The drive waveform is adequate to actuate the scratch drive actuator, but does not disturb the steering arm, regardless of whether the arm is in its raised or lowered position. For this reason, the same drive waveform can be applied either when the device is going straight or when it is turning. The behavior of the device is changed only by the position of its stylus. Further details regarding the design of the drive waveform are provided in Section 5, and also in Appendix C.

Before the micro-robot can turn, the stylus at the tip of its steering arm must be lowered into contact with the substrate. When the stylus is lowered, it creates friction at the contact point, causing the device to turn. Then, the drive waveform is applied. The frictional force acting on the stylus as the scratch drive actuates causes the device to turn. If the maximum available force of friction on the stylus exceeds the force applied on it by the scratch drive, then the stylus will not move, and the device will pivot around it.

There are two considerations that must be taken into account in the design of the steering arm. First, the arm must be stiff enough that the peak voltage of the drive waveform (112 V) does not inadvertently pull it into contact with the substrate.

Second, it must be flexible enough that, once in contact, the minimum voltage of the drive waveform (39 V) does not allow it to release from the substrate. The voltage at which the beam will snap down into contact with the electrodes is called the *snap-down voltage*. When the voltage is subsequently decreased, the tip of the cantilever will remain in contact with the substrate until another instability is reached, and it snaps upward. This latter instability is known as the *release voltage*.

The steering arms on the micro-robots presented in this paper have snap-down and release voltages of approximately 60 V, and 15 V, respectively. [1] In this way, the stylus can be raised and lowered at will, independent of forward motion. This allows the power delivery waveform to be used both to control the state of the arm as well as to provide energy to propel the device forward. Further details of the design of the steering arm are provided in Appendix D.

5 Control

This section describes the instruction set of the MEMS micro-robots, and shows how to encode it in a control waveform to specify device behavior. The devices presented in this paper can, at any given time, be in one of the four distinct states shown in Figure 3. The stylus can be either up or down, and the scratch drive can be either flexed or relaxed.

We can now define four voltages that comprise the instruction set of the micro-robot. We have:

$\mathbf{V_1 = 0\ V}$	$\mathbf{V_2 = 39\ V}$	$\mathbf{V_3 = 112\ V}$	$\mathbf{V_4 = 140\ V}$
Raises Steering Arm Relaxes Scratch Drive	Relaxes Scratch Drive	Flexes Scratch Drive	Lowers Steering Arm Flexes Scratch Drive

To be able to operate the scratch drive independently of the position of the stylus, we need the drive waveform to fit within the voltage range defined by the steering arm's snap-down and release voltages. Since V_2 and V_3 fall between the snap-down and release voltages of the steering arm, application of these two voltages will not change the state of the steering arm actuator.

With these four instructions, we can model the system as the finite state machine shown in Figure 3. Here, the set of discrete DC voltages, $\{V_1, V_2, V_3, V_4\}$ comprises the transitions, and the zero-voltage state, S_0, is the start state. The pair of voltages, (V_2, V_3) comprises the drive waveform discussed in Section 4. The blue and red transitions in Figure 3 correspond to the two motion operations of the device that can occur when the drive waveform is applied.

It is easy to see from this state transition diagram that all four system states can be reached, and to compute the voltage sequence required to achieve each one. This leads directly to the control waveforms shown in Figure 4. Both waveforms begin by selecting the system state associated with the desired motion, and then applying the drive waveform. After 250 steps, the waveform polarity is reversed to minimize charge-trapping in the dielectric. The desired state is refreshed, and then the drive waveform is continued.

[1] These values correspond to electrode-to-electrode voltages of 120 V and 30 V, respectively.

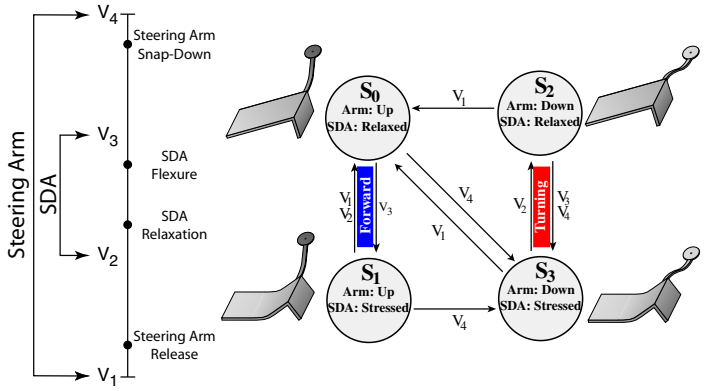

Fig. 3. The state transition diagram of the micro-robot. Four voltages, $V_1 < V_2 < V_3 < V_4$, are used in constructing control waveforms. SDA = untethered scratch drive actuator.

The control system can be extended to include an arbitrary number of states. Further details regarding the extensibility of the control system are provided in Appendix E.

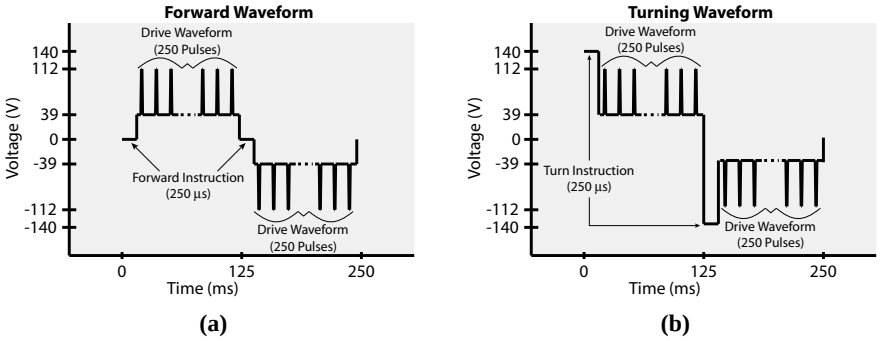

Fig. 4. Control waveforms used for driving the micro-robots at a stepping frequency of 4 kHz. **a:** The forward waveform lowers the device voltage to zero before initiating the drive waveform, ensuring that the steering arm will be in the raised position. **b:** The turning waveform increases the device voltage to 140 V (or -140 V) before initiating the drive waveform, ensuring that the steering arm will be in the lowered position. The polarity of the control waveform is reversed every 250 pulses to limit the effects of parasitic charging. The state of the steering arm is refreshed each time this occurs. In the control waveform segments shown here, the instructions are refreshed at 0 and 125 ms, when the polarity of the control waveform is reversed.

6 Performance

We tested the performance of the micro-robots in a variety of ways. First, we examined the reliability of the two motion primitives (forward motion and turning)

Table 1. Turning rate of individual devices at 4 kHz stepping frequency.

	Open-Loop Turning Rate (std. dev.) [degrees/mm]				
Signal	**Device 1**	**Device 2**	**Device 3**	**Device 4**	**Device 5**
Forward :	-14.6 (7.8)	9.7 (9.6)	7.8 (14.9)	-21.7 (10.5)	0.4 (13.6)
Turning :	353 (4.9)	338 (4.6)	250 (9.7)	365 (6.5)	321 (8.1)

with ten test runs of each motion primitive for each of five test devices. Second, we looked at how the radius of curvature can be controlled by time-sequence multiplexing the motion primitives. Third, we demonstrated teleoperated control of the devices by piloting them through clockwise and counter-clockwise rectangular paths. Last, we demonstrated device endurance by continuous operation in turning mode until accumulated error forced the device off of the operating environment.

This section quantifies results from 271 open-loop test runs of five devices, and presents representative segments of additional paths traversed during teleoperation. In all of these test runs, the devices were run under an optical microscope while recording their motions with a digital video camera. Device headings and positions were later extracted by image analysis with precision of $\pm 2^\circ$ and $\pm 1.6\ \mu\mathrm{m}$ respectively. The position of the device was defined at the center of the scratch drive plate, and its heading was defined by the orientation of the scratch drive bushing.

To test the forward motion, each of five devices was operated with the waveform shown in Figure 4a for 10 10-second trials with a 4 kHz stepping frequency, during each of which the devices traveled an average of 566 $\mu\mathrm{m}$. For consistency, all of these trials were run approximately parallel to the electrodes. The turning rate of an individual test run is defined by the slope of the best-fit line to the device heading over the course of the test run, plotted as a function of distance traveled.

Figure 5a shows turning rates for all ten forward test runs of one device. Over all devices, the average turning rate was $-3.7^\circ/\mathrm{mm}$, with a standard deviation of $13.9^\circ/\mathrm{mm}$. Average turning rates for individual devices are shown in Table 1, with standard deviations in parentheses. The errors shown accumulated open-loop, in the absence of an error-correcting scheme, and can be corrected through closed-loop control.

To test the turning motion, the devices were operated with the waveform shown in Figure 4b with a stepping frequency of 4 kHz for 10 trials of one full revolution each. Figure 5b shows the deviation from initial heading for all test runs of one of these devices. For all devices combined, the average turning rate was $325^\circ/\mathrm{mm}$, which corresponds to a radius of curvature of 176 $\mu\mathrm{m}$. The standard deviation of the turning rate across all 4 kHz turning runs of all devices was $45.3^\circ/\mathrm{mm}$. Standard deviations for individual devices are considerably lower, and appear in Table 1.

The forward and turning behaviors can be combined to produce turning radii with intermediate values. To demonstrate this, we drove a device with a signal composed of turning waveforms interleaved with forward waveforms, at a stepping frequency of 8 kHz. We tested waveforms with ratios of 50% turning and 75% turning, and compared these to the results of the test runs with 100% turning described above. There were ten full-revolution test runs at each of these turning ratios. Figure 5.c

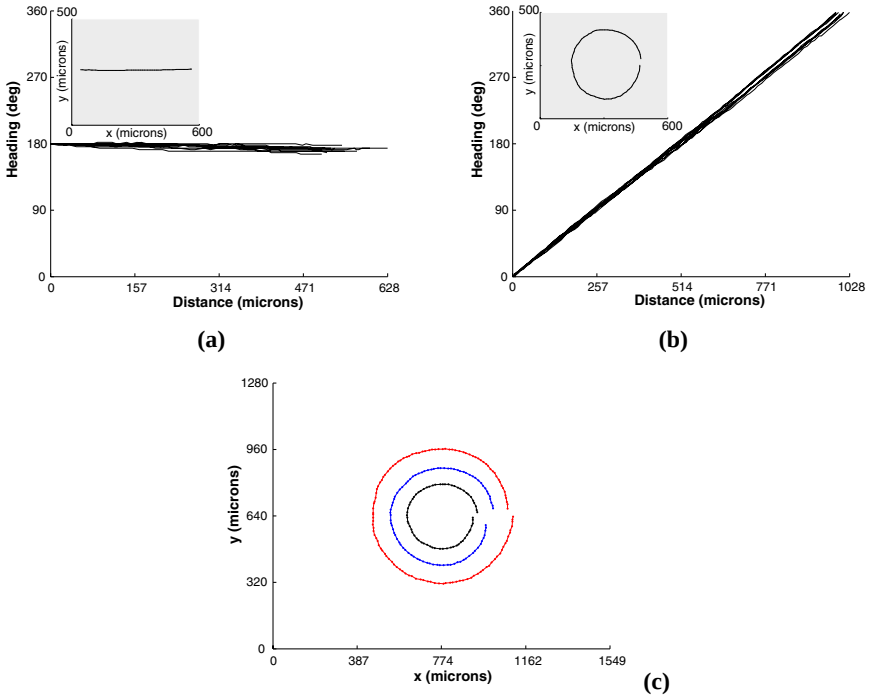

Fig. 5. Open-loop test runs of an electrostatic MEMS micro-robot. **a:** The change in device heading over the course of each of ten trials with the forward waveform at a stepping frequency of 4 kHz. The inset shows a representative path traversed by the device during one of the ten trials. The average turning rate for these trials was $-14.6^\circ/\mathrm{mm}$. **b:** Device heading as a function of distance for each of ten trials with the turning waveform at a stepping frequency of 4 kHz. The inset shows a representative path. The average turning rate was $353^\circ/\mathrm{mm}$, corresponding to a radius of curvature of 162 μm. **c:** Representative paths traversed by a device with waveforms composed of different amounts of turning and forward control signals. In red: 50% turning. In blue: 75% turning. In black: 100% turning.

shows sample paths from tests runs executed at 50%, 75%, and 100% turning ratio, along with a plot of curvature vs. turning ratio averaged across all trials. The devices have been experimentally shown to achieve speeds in excess of 200 μm/s, with an average step-size of 12 nm. (See Appendix F for more details)

With a human operator observing the device behavior, and controlling the waveforms sent to the device, it is possible to direct the devices through teleoperation. Figure 6 shows clockwise and counter-clockwise rectangular paths traversed by one of these devices under teleoperated control. Digital videos of our devices are available on-line here [15].

For additional tests regarding the reliability of the device see Appendix G.

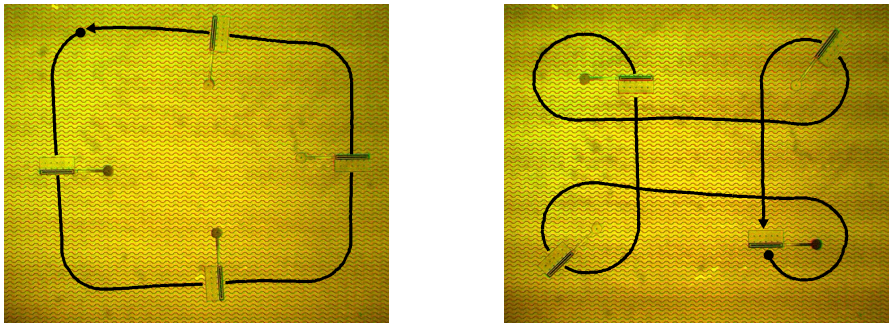

Fig. 6. Sample paths traversed by one of the micro-robots under teleoperated control. **Left:** Traversal of a counter-clockwise rectangular path by turning corners at minimum turning radius. **Right:** Clockwise paths were achieved by looping at the corners.

7 Conclusions

This paper presented an electrostatic MEMS micro-robot that is 1 to 2 orders of magnitude smaller than previous micro-robotic systems. This device was shown to perform in a robust and repeatable manner, and could be controlled through teleoperation to traverse complex paths.

The devices are powered through a capacitive coupling with an interdigitated electrode array, so that the devices need not be restricted by the wires and rails that power most electrostatic MEMS devices. Careful design of the mechanical structure of the micro-robot body allows the power signal to double as the control signal. The control information received from this signal is stored as electro-mechanical state information on-board the robot, so that the device can exhibit different behaviors in response to the same drive waveform, based on a previously-encoded state.

The communication and control system utilized in these micro-robots exploits electromechanical hysteresis to store state information within the micro-robot body, and is analogous to a four-state finite state machine. Useful extensions to the complexity of the control system could include the ability to turn in both directions, to move in “reverse”, or to manipulate other objects in the environment. One particularly interesting extension would be the parallel operation of multiple micro-robots for cooperative tasks.

8 Acknowledgements

This work was supported by award number 2000-DT-CX-K001 to B.R.D., from the Office for Domestic Preparedness, Department of Homeland Security, USA. The electron micrographs were taken at the Ripple Electron Microscopy Laboratory, with the help of Chuck Daghlian. The vacuum microprobe used for device transport was developed with the help of Richard Rohl and the National Science Foundation’s Research Experience for Undergraduates program. We thank Ursula Gibson for the use of equipment in her lab, and for many helpful discussions. We also thank Devin Balkcom, Karl Böhringer, Jessica Gomez, and Satish Prabhakaran for their advice and suggestions.

References

1. S. Baglio, S. Castorina, L. Fortuna, and N. Savalli. Development of autonomous, mobile micro-electro-mechanical devices. In *IEEE International Symposium on Circuits and Systems. Proceedings*, volume IV, pages 285–288, 2002.
2. P. Basset, A. Kaiser, P. Bigotte, D. Collard, and Lionel Buchaillot. A large stepwise motion electrostatic actuator for a wireless microrobot. In *Proceedings of the IEEE International Conference on Micro Electro Mechanical Systems*, pages 606–609, 2002.
3. Paul E. Kladitis and Victor M. Bright. Prototype microrobots for micro-positioning and micro-unmanned vehicles. *Sensors and Actuators A (Physical)*, A80(2):132–137, March 2000.
4. Richard Yeh, Ezekiel J. J. Kruglick, and Kristofer S. J. Pister. Surface-micromachined components for articulated microrobots. *Journal of Microelectromechanical Systems*, 5(1):10–17, March 2001.
5. S. Hollar, A. Flynn, C. Bellew, and K. S. J. Pister. Solar powered 10 mg silicon robot. In *The Sixteenth Annual International IEEE Conference on Micro Electro Mechanical Systems, Proceedings*, pages 706–711, January 2003.
6. Bruce R. Donald, Christopher G. Levey, Craig D. McGray, Daniela Rus, and Mike Sinclair. Power delivery and locomotion of untethered micro-actuators. *Journal of Micro-Electromechanical Systems*, 12(6):947–959, December 2003.
7. Bruce R. Donald, Christopher G. Levey, Craig D. McGray, Daniela Rus, and Mike Sinclair. Untethered micro-actuators for autonomous micro-robot locomotion: Design, fabrication, control, and performance. In *11th International Symposium of Robotics Research (ISRR), Proceedings*, pages 19–22, October 2003.
8. H. Hermes. On local and global controllability. *SIAM Journal of Control*, 12:252–261, 1974.
9. K. W. Markus, D. A. Koester, A. Cowen, R. Mahadevan, V. R. Dhuler, D. Roberson, and L. Smith. MEMS infrastructure: The multi-user MEMS processes (MUMPs). In *Proceedings of the SPIE - The International Society for Optical Engineering, Micromachining and Microfabrication Process Technology*, volume 2639, pages 54–63, 1995.
10. P. Dario, R. Valeggi, M. C. Carrozza, M. C. Montesi, and M. Cocco. Microactuators for microrobots: a critical survey. *Journal of Micromechanics and microengineering*, page 141, September 1992.
11. K. Kotay and D. Rus. Locomotion versatility through self-reconfiguration. *Robotics and Autonomous Systems*, 26:217, 1999.
12. Bruce. R. Donald. *MEMS for Infosecurity*. Award Number 2000-DT-CX-K001, The Office for Domestic Preparedness, Department of Homeland Security, USA, 2000-2006.
13. S. Baglio, S. Castorina, L. Fortuna, and N. Savalli. Technologies and architectures for autonomous "MEMS" microrobots. In *IEEE International Symposium on Circuits and Systems. Proceedings*, volume II, pages 584–587, 2002.
14. Hirofumi Miura, Takashi Yasuda, Yayoi Kubo Fujisawa, and Isao Shimoyama. Insect-model based microrobot. In *Transducers*, pages 392–395, June 1995.
15. Bruce Donald, Christopher Levey, Craig McGray, Igor Paprotny, and Daniela Rus. An untethered, electrostatic, globally-controllable MEMS micro-robot. supplementary videos. Technical Report TR2005-553, Dartmouth College, `www.cs.dartmouth.edu/reports/abstracts/TR2005-553/`, 2005.

Appendix

Appendix **A** describes in detail the fabrication process used to manufacture the micro-robots and the electrical grids. In appendix **B** we provide an extended description of the power delivery mechanism. Appendix **C** describes the construction of the drive waveform used to locomote our micro-robots. In appendix **D** we provide an analysis of the design parameters used to define the steering arm, and the steering waveform. Appendix **E** discusses the extensibility of the control system. Appendix **F** contains data on device speed and step-size. In appendix **G** we summarize a reliability test of prolonged device operation. Please note that the appendix contains an additional reference section.

A Details of the Fabrication Process

The first steps in fabricating the devices were performed through the PolyMUMPs process [9]. This multi-user surface micromachining process consists of three layers of polycrystalline silicon, separated by two sacrificial layers of phosphosilicate glass. The untethered scratch drive actuators and steering arms are both formed from the top layer of polysilicon, as shown in Figure 7.

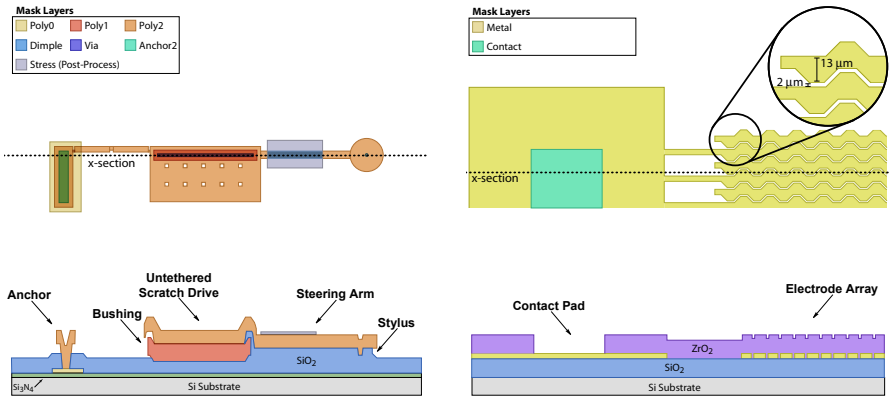

Fig. 7. Fabrication of electrostatic micro-robots. **Left:** Layout and cross-section of an electrostatic micro-robot just prior to sacrificial release. The device utilizes the first and second released polysilicon layers from the PolyMUMPs process [9], plus an additional layer added during post-processing. This layer consists of 830 Å of chromium with a tensile residual stress of approximately 550 MPa, and is lithographically patterned with the "Stress" mask (gray, above). After release, the stress in this layer curls the steering arm out of plane. **Right:** Layout and cross-section of the electrical grids used as the micro-robots' operating environments. The first mask layer defines the metal electrodes, while the second layer defines contact holes through the electrode insulation. The metal electrodes are sandwiched between a layer of thermal silica, and a deposited layer of zirconium dioxide.

The bushing is formed by combining the conformalities that result from the PolyMUMPs Dimple Etch and Via Etch, and is approximately 1.5 μm high. Similarly,

the stylus at the end of the steering arm is formed from the Dimple Etch conformality, and is 0.75 μm high. After the PolyMUMPs process is complete, we coat the devices with a patterned layer of evaporated chromium. The tensile residual stress in the chromium curves the steering arms upwards. This curvature allows the arm to remain suspended above the substrate, even when sufficient voltage is applied to actuate the scratch drive.

The electrical grids used as operating environments for the devices were fabricated entirely in-house, and consist of an array of metal interdigitated electrodes on a silicon substrate. The electrodes are insulated from the substrate by a 3 μm-thick layer of thermal silica, and are coated with 0.5 μm of zirconium dioxide, followed by a 300 Å passivation layer of evaporated silica. This dielectric layer allows power delivery to devices placed on top of the electrical grids by capacitive coupling with the underlying electrodes. Fabrication of these electrical grids is illustrated in Figure 7. Once fabrication is complete, the devices are transferred onto the grids with a vacuum microprobe. Processing details regarding the fabrication of the devices and the electrical grids are presented in Appendices A.1 and A.2.

A.1 Actuator Fabrication

Figure 7 shows the layout of one of the devices. The scratch drive plate is 1.5 μm thick, and is defined by a 120 μm by 60 μm rectangle on the third polysilicon layer (Poly2) of the PolyMUMPs process. The scratch drive bushing is 1.5 μm high, and is composed of a Dimple Etch conformality beneath a sheet of Poly1 that is anchored to the Poly2 layer with the Poly1-Poly2-Via etch. The steering arm is 133 μm long, 8 μm wide, and has an 18-μm-radius disc at its tip. A stylus is defined in the center of this disc by a 1.5-μm-radius dimple that protrudes 0.75 μm beneath the bottom surface. The base of the steering arm is curled so that the tip of the arm is approximately 7.5 μm higher than the scratch drive plate. Since the PolyMUMPs process does not include a layer with enough stress to create this curvature, a layer of tensile chromium is deposited and patterned in the following post-processing sequence.

The devices are received from the foundry on 1-cm^2 silicon die. After the protective coating of photoresist is removed, the die are soaked in buffered hydrofluoric acid to under-etch the top polysilicon layer. This produces a re-entrant surface profile which enables lift-off of subsequent layers.

After rinsing and drying, the die are coated with 830 Å of chromium by thermal evaporation. As deposited, the chrome has an intrinsic tensile residual stress of approximately 550 MPa, which will produce the necessary curvature in the steering arms upon sacrificial release. The chrome is lithographically patterned with the "Stress" layer, shown in Figure 7, and etched in a perchloric-acid-based chrome etchant to transfer the pattern.

Once the chrome pattern has been defined, the sacrificial release etch is performed by soaking in 49% hydrofluoric acid. In addition to releasing the polysilicon structures, this undercuts the excess chrome and detaches it from the substrate. After rinsing in DI water, the die are dehydrated by soaking in isopropyl alcohol, and are then transferred to an ozone-friendly fluorocarbon solvent (based on 2,3-

dihydrodecafluoropentane and isopropanol). Slow removal from this solvent ensures very little spotting or unnecessary stiction.

The devices are initially attached to substrate anchors by notched sacrificial beams. These beams are broken with a tungsten microprobe tip to release the devices, as described in [6, p. 951], prior to transferring them to the power-delivery substrates with a vacuum microprobe.

A.2 Substrate Fabrication

Figure 7 shows the layout of one of the electrical grids used as operating environments for the micro-robots. These grids consist of interdigitated metal electrodes microfabricated on oxidized silicon substrates. An insulating coating of zirconium dioxide provides a high-impedance dielectric coupling between the electrodes and the devices. Fabrication of these electrical grids was accomplished with the following process sequence.

The sequence begins with a set of 3-inch $\langle 100 \rangle$ n-type (phosphorus-doped) silicon wafers. The wafers are cleaned, and oxidized for 20 hours at 1100° C in oxygen, followed by an additional 14 hours of wet oxidation using water vapor in a nitrogen carrier gas.

After cooling, the wafers are patterned with the "Metal" pattern shown in Figure 7, using a bi-layer photodefinable resist suitable for liftoff. Metallization is then conducted by resistive boat evaporation at 10^{-6} Torr. Three metal layers are evaporated onto the patterned substrates. The middle layer consists of 500 Å of gold, and serves as the conductive bulk of the electrodes. Above and below this are two layers of chromium, each 50 Å thick, which serve as adhesion layers between the gold, the oxidized substrate, and the zirconium dioxide which will be subsequently deposited to insulate the electrodes.

After metallization, each wafer is cleaved into four 1-inch die. These die are sonicated in photoresist stripper at 45° C, to lift off the resists and unwanted metal, leaving only the interdigitated electrodes and their associated contact pads. To insulate the electrodes, the die are then coated with 5100 Å of zirconium dioxide, deposited by electron beam evaporation from zirconia powder according to the protocol described in [16]. The process used for zirconia deposition is critical to the quality of the dielectric, and to device performance. Since ZrO_2 dissociates during evaporation, it is important to facilitate recombination at the substrate surface. To do so, the substrates are heated to 100° C, and oxygen gas is introduced into the chamber to a pressure of 10^{-4} Torr. Throughout the deposition process, the chamber pressure is maintained to within $\pm 10\%$ by manually adjusting the oxygen flow. When the zirconia deposition is complete, the chamber is pumped back down to 2×10^{-6} Torr, and a 300 Å silica layer is then evaporated. We have found empirically that this over-layer of silica improves the walking performance of scratch drive actuators on zirconia-insulated substrates.

Once the die have been insulated, they are patterned with the "Contact" mask shown in Figure 7, and etched in a 5:1 buffered hydrofluoric acid solution for 5 minutes. This etches through the zirconia insulation, stopping on the contact pads.

After rinsing and drying, the substrates are ready for use. The devices are transferred to the electrode arrays by vacuum microprobe, and tungsten-tipped microprobes are used to provide power to the interdigitated electrodes. In the next section, we discuss the delivery of electrical power from these insulated arrays of electrodes to untethered MEMS devices.

B Detailed Explanation of the Power Delivery Mechanism

When a conductive actuator, such as a scratch drive, rests on top of these electrodes, it forms the capacitive circuit shown in Figure 8. In this way, a voltage is applied to the actuator, regardless of its position and orientation relative to the underlying electrodes (i.e. no position-restricting wires or tethers are required.)

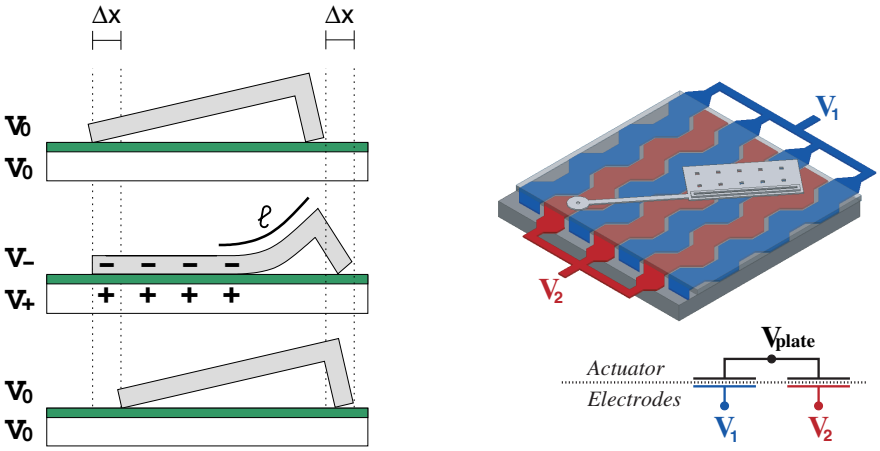

Fig. 8. Left: A schematic of the operation of a tethered scratch drive actuator [17,18]. The length of the curved region of the plate, ℓ, and the step size, Δx, are determined by the voltage. **Right:** A schematic of a capacitively-coupled power delivery mechanism for untethered actuators [6]. The potential induced on the actuator, V_{plate}, is approximately the mean of V_1 and V_2.

Once a voltage has been applied to a scratch drive actuator as described above, the actuator will deform as shown in Figure 8 [17,19]. Hayakawa *et. al.* [20] have calculated the length of the curved region of the scratch drive, ℓ, as follows:

$$\ell = \left(\frac{3Et^3h^2d}{4\kappa\epsilon_0 V^2} \right)^{\frac{1}{4}} \tag{1}$$

where κ is the dielectric constant of the insulator, ϵ_0 the permittivity of free space, h the bushing height, V the applied voltage, E the Young's modulus of the plate material, d the insulator thickness, and t the thickness of the actuator plate. When the voltage is decreased, the flexure in the scratch drive plate relaxes, as shown in

Figure 8. Each time the voltage is cycled, the scratch drive moves forward by a small increment, known as the *step size*. The frequency at which this cycle occurs is known as the *stepping frequency*, and the speed of the actuator is the product of its stepping frequency and its average step size.

Equation (1) shows that there is a trade-off between voltage, insulator thickness, and the relative permittivity of the dielectric. Hence, to improve device performance at a given voltage, we would like an insulator with a high value of κE_{br}, where E_{br} is the dielectric strength. For this reason, the high-κ dielectrics under investigation by the semiconductor industry [21] should also be good materials to use as the insulating layer in contact-mode electrostatic MEMS. One such material that performs well in this regard is e-beam-evaporated zirconium dioxide.

To deliver power to our MEMS micro-robots, we have used insulated substrates covered with zirconia-insulated gold electrodes. The edges of the electrodes are jagged (as shown in Figures 1 and 7) to help maintain a consistent voltage on the actuator, regardless of the actuator's pose. The electrodes are thin enough that the capacitance between adjacent electrodes is negligible, so the largest source of parasitic capacitance is between the electrodes and the underlying silicon substrate. This was sufficiently small for the purposes of the experiments conducted in this paper, and could easily be made much smaller by replacing the silicon substrate with an insulating material such as quartz, or with silicon-on-insulator (SOI) techniques. With these parasitic capacitances removed, the bulk of the delivered power can be focused only on those areas where a device is present.

C Construction of the Drive Waveform

One important parameter in the operation of a scratch drive actuator is the peak voltage of the drive signal. This has been studied by [22] and [23]. They showed correct operation of scratch drive actuators with drive signals having a peak voltage as low as 60 V between the scratch drive plate and an underlying electrode. This minimum operating voltage is particularly important when using a scratch drive actuator as the propulsion system in a steerable micro-robot, since any voltage that is too high will inadvertently pull the device's stylus into contact with the substrate. Similarly, any voltage that is too low can inadvertently release the stylus from contact with the substrate. We would like to choose a waveform for actuating the scratch drive that will not effect the state of the steering arm.

We tested an untethered scratch drive that was 60 μm long, 120 μm wide, and had a 1.5-μm-high bushing. We operated this untethered scratch drive on one of the zirconia-insulated environments described above, with a 120-ms waveform, consisting of 250 positive 60-μs pulses, followed by 250 negative pulses with a duty cycle of 25%. We examined the performance of the device as a function of both the peak voltage of the pulses, and the minimum voltage of the pulses. We found that the peak voltage of the pulses applied between adjacent electrodes must be at least 60 ± 10 V to produce motion in the scratch drive, corresponding to approximately 30 ± 5 V between the scratch drive and each electrode. The minimum required peak voltage was consistent for pulses with minimum voltages of 0 V, 20 V, and 40 V.

However, when the minimum voltage of the pulse was raised to 60 V, the device failed to operate with any peak voltage below and including 100 V.

Given the fairly wide range of acceptable drive waveforms, we selected a pulsed wave with peak voltage of 112 V and minimum voltage of 39 V, applied between the electrodes. This corresponds to peak and minimum pulse voltages between the device and the electrodes of approximately 56 V and 19 V, respectively. This drive waveform is adequate to actuate the scratch drive actuator, but does not disturb the steering arm, regardless of whether the arm is in its raised or lowered position.

Since the voltage on the device must be maintained above zero for considerable lengths of time, it is possible for static charge to accumulate in trap sites within the electrode insulation [24-26]. Three characteristics of our chosen drive waveform help to minimize this effect. First, the polarity of the drive waveform is reversed every 250 pulses. Second, the duty cycle of the waveform is kept small. In all of our test runs, the high-voltage pulse of the drive signal is 10 μs wide at its peak, 30 μs wide at its base, and has linear ramps for a full-width-half-max pulse width of 20 μs. Depending on the stepping frequency at which we operate the devices (2 kHz, 4 kHz, 8 kHz, or 16 kHz), this corresponds to a duty cycle of 4-32%. Third, the peak voltage of the drive signal (112 V) is considerably higher than the 60 V required for operation. Our experience suggests that devices driven with peak voltages close to the minimum required voltage will fail after a short period of operation. However, with the higher peak voltage, the devices can operate for hours without failure.

D Design of the Steering Arm Actuator

The snap-down voltage of a cantilever beam is one of the earliest problems studied in the field of MEMS. First presented by Nathanson *et. al.* in 1967 [27], the electromechanical analysis of cantilever snap-down has since been refined in numerous papers [28-31]. For simplicity, we will use Nathanson's model here.

Nathanson used a lumped energy minimization model to calculate the snap-down voltage of a cantilever beam as follows:

$$V_{SD} \approx \sqrt{\frac{8Kg_0^3}{27\epsilon_0 A}} \tag{2}$$

where K is the spring constant of the cantilever beam, g_0 is the zero-voltage gap between the cantilever and the electrode, and A is the total area of the cantilever. A similar analysis can be used to calculate the release voltage:

$$V_R \approx \sqrt{\frac{2Kg_1^2\left(g_0 - g_1\right)}{\epsilon_0 A}} \tag{3}$$

where g_1 is the contact gap between the cantilever and the electrode, as defined, for example, by a dimple.

These values are, of course, somewhat approximate, but they serve to illustrate the following interesting limitation. As mentioned earlier, we would like the micro-robot's steering arm to have a high snap-down voltage, and a low release voltage. In

other words, we would like to be able to increase the ratio of the snap-down voltage to the release voltage. We'll call this the *snap ratio*. From the above two equations, the snap ratio is as follows:

$$R_s = \frac{V_{SD}}{V_R} \approx \sqrt{\frac{4g_0^3}{27g_1^2\left(g_0 - g_1\right)}} \tag{4}$$

We note that the snap ratio is independent of the beam's spring constant and area, but depends strongly on the gaps g_0 and g_1.

Due to the largely planar nature of current microfabrication techniques, it can be difficult to parameterize z-axis geometries such as a cantilever's zero-voltage gap, without introducing a new processing step (e.g. a new material layer or etch mask) for each desired parameter value. One way to be able to parameterize these z-axis geometries is to deform parts out-of-plane using stress gradients of bi-layer materials. Tsai *et. al.* presented a general technique for controlling part curvature, using a top layer of silicon nitride with tensile residual stress [32,33]. We have adapted this approach for use with a chromium stress layer as described in Appendix A.1.

By curving the steering arm out-of-plane, we can increase the snap-down voltage well above the peak voltage of the scratch drive actuator's drive waveform, while keeping its release voltage well below the minimum of the drive waveform.

E Control System Extensibility

Consider a class of n-component electromechanical devices, in which each component can have one of two possible states. We'll call these states 0 and 1. States of the system as a whole can then be identified with n-bit binary numbers.

Let $C = \{c_1, \ldots, c_n\}$ be an n-component system where each component, $c_i \in C$, has a binary state and two unique control voltages: $D(c_i)$ and $R(c_i)$. Let this system perform as follows. If the voltage on the system is raised above $D(c_i)$, the component c_i will switch to state 1. If the voltage on the system is lowered below $R(c_i)$, the component will switch to state 0. If the voltage on the system is set to any value between $D(c_i)$ and $R(c_i)$, then the state of the component will maintain whatever value it held before the new voltage was applied. $D(c_i)$, for example, could be the snap-down voltage of a cantilever beam, while $R(c_i)$ could be the release voltage. The voltage range between $D(c_i)$ and $R(c_i)$ denotes the *hysteresis band* of the i^{th} component.

It is necessary and sufficient that the hysteresis bands of all components be *nested*. For any two components c_i and c_j, if both $R(c_i) < R(c_j)$ and $D(c_j) < D(c_i)$ hold, then it is simple to select any desired system state. To do so, begin by setting the state of the outermost component in the nesting (i.e. the component with the largest value of $D(c_i)$), and then progress inward.

To demonstrate this control strategy in a more complex system, we built an electromechanical finite state machine (FSM) that consists of three independently-controllable cantilevers that together define eight different possible states. An electron micrograph of the FSM is shown in Figure 9.

The state of each cantilever is assigned the value 1 if the cantilever is in contact with the substrate, and 0 if the cantilever is not in contact. The state of the FSM as a whole can then be described as a binary number ranging from 000 to 111.

The snap-down voltages of these beams were found to be approximately 120 V, 140 V, and 160 V, with release voltages of approximately 90 V, 40 V, and 10 V, respectively.

Based on these values, we selected a set of 6 voltages to control the finite state machine: { 0, 32, 76, 136, 152, 164 } (all units in volts).

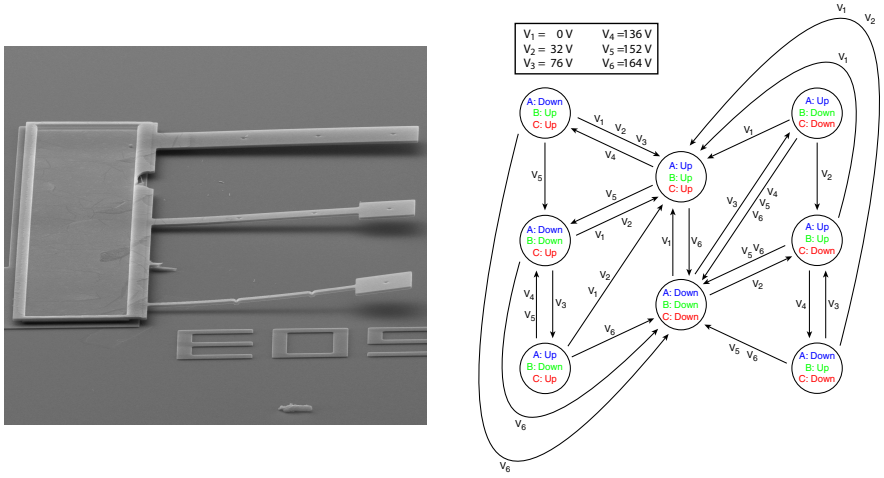

Fig. 9. An eight-state electromechanical finite-state machine (FSM). **Left:** The FSM consists of three cantilever beams with parameterized width and curvature, as shown in this electron micrograph. All three cantilevers are electrically connected, and must all have the same voltage at any given time. **Right** The state transition diagram of the FSM. The control voltages (inset, upper left) are chosen from the snap-down and release voltages of each of the individual cantilevers. Since these three voltages pairs nest within one another, there is a sequence of voltages that will cause the system to transition between any two states.

To demonstrate the correct operation of this finite state machine, we traversed the shortest paths from the start state (000) to each of the other seven states the state transition diagram shown in Figure 9. These seven paths were repeated three times in sequence, without deviation from the system states predicted by the state transition diagram.

F Speed and Step-size Data

Table 2 presents the speed of 5 devices using a stepping frequency of 2,4,8 and 16 KHz. The maximum recorded device speed was 224 μm/s, using a stepping frequency of 16 KHz. The step-size can be obtained by dividing the measured speed

Table 2. Speed of individual devices.

Signal	Open-Loop Speed (std. dev.) [μm/sec]				
	Device 1	**Device 2**	**Device 3**	**Device 4**	**Device 5**
Forward (4 kHz):	55 (4.4)	58 (2.7)	55 (5.9)	49 (4.0)	66 (2.6)
Turning (2 kHz):	25 (0.3)	28 (0.7)	24 (0.8)	16 (0.4)	29 (0.6)
Turning (4 kHz):	51 (0.8)	53 (0.5)	47 (1.2)	34 (1.0)	59 (0.7)
Turning (8 kHz):	80 (7.6)	93 (1.7)	97 (4.7)	70 (1.1)	105 (2.2)
Turning (16 kHz):	224 (2.9)	147 (1.7)	204 (7.4)	133 (1.3)	197 (6.0)

by the frequency of the drive waveform. The step-sizes for the experiments displayed in Table 2 range from 8 nm to 16 nm, with an overall average step-size of 12 nm.

G Reliability Testing of Device Operation

For all experiment described in Section 6 and below, the humidity was maintained at below 15% RH by a continuous stream of dry nitrogen. Drive waveforms were produced using an Agilent 33120A arbitrary waveform generator, and amplified with a Trek PZD700-1 high-voltage power amplifier with a gain of 200.

To test the reliability of the devices during prolonged operation, we operated one device until the point of failure. The device was piloted to the center of the operating environment, and the turning waveform was applied at a stepping frequency of 4 kHz. Over the course of the next seventy-five minutes, the device executed 215 full rotations, open-loop, without operator intervention, for a total distance traveled of over 35 centimeters. The device eventually stopped when accumulated position error forced it off of the 2.5-mm-wide operating environment. When the device was pushed back onto the operating environment with a microprobe, it continued to operate correctly.

Refs. 1-15 are in the main text on pages 10-11

References

[16] J. A. Dobrowolski, P. D. Grant, R. Simpson and A. J. Waldorf, "Investigation of the Evaporation Process Conditions on the Optical Constants of Zirconia Films," *Applied Optics*, vol. 28, no. 18, pp. 3997–4005, 1989.

[17] T. Akiyama and K. Shono, "Controlled Stepwise Motion in Polysilicon Microstructures," *Journal of Microelectromechanical Systems*, vol. 2, no. 3, pp. 106–110, 1993.

[18] T. Akiyama, D. Collard and H. Fujita, "Scratch Drive Actuator with Mechanical Links for Self-Assembly of Three-Dimensional MEMS," *Journal of Microelectromechanical Systems*, vol. 6, pp. 10–17, 1997.

[19] T. Akiyama, D. Collard and H. Fujita, "A quantitative analysis of Scratch Drive Actuator using buckling motion," in *IEEE International Conference on Micro Electro Mechanical Systems. Proceedings*, January 1995, pp. 310–315.

[20] K. Hayakawa and A. Torii and A. Ueda, "An Analysis of the Elastic Deformation of an Electrostatic Microactuator," *Transactions of the Institute of Electrical Engineers of Japan, Part E*, vol. 118-E, no. 3, pp. 205–211, March 1998.

[21] T. P. Ma, "Opportunities and Challenges for High-k Gate Dielectrics," in *2004 IEEE International Symposium on the Physical and Failure Analysis of Integrated Circuits. Proceedings*, pp. 1–4.

[22] L. Li, J. G. Brown and D. Uttamchandani, "Detailed Study of Scratch Drive Actuator Characteristics Using High-Speed Imaging," in *Proceedings of the SPIE. Reliability, Testing, and Characterization of MEMS/MOEMS*, vo. 4558, 2001, pp. 117–123.

[23] R. J. Linderman and V. M. Bright, "Optimized Scratch Drive Actuator for Tethered Nanometer Positioning of Chip-Sized Components," *Transducers*, June 2000, pp. 214–217.

[24] W. M. van Spengen, R. Puers, R. Mertens and Ingrid De Wolf, "A Comprehensive Model to Predict the Charging and Reliability of Capacitive RF MEMS Switches," *Journal of Micromechanics and Microengineering*, vol. 14, pp. 514–521, 2004.

[25] J. Wibbeler, G. Pfeifer and M. Hietschold, "Parasitic Charging of Dielectric Surfaces in Capacitive Microelectromechanical Systems (MEMS)," *Sensors and Actuators A*, vol. 71, pp. 74–80, 1998.

[26] C. Cabuz, E. I. Cabuz, T. R. Ohnstein, J. Neus and R. Maboudian, "Factors Enhancing the Reliability of Touch-Mode Electrostatic Actuators," *Sensors and Actuators A*, vol. 179, pp. 245–250, 2000.

[27] H.C. Nathanson, W. E. Newell, R. A. Wickstrom and J. R. Davis, "The Resonant Gate Transistor," *IEEE Transactions on Electron Devices*, vol. 14, pp. 117–133, 1978.

[28] P. M. Osterberg and S. D. Senturia "M-TEST: A Test Chip for MEMS Material Property Measurement Using Electrostatically Actuated Test Structures," *Journal of Microelectromechanical Systems*, vol. 6, no. 2, pp. 107–118, 1997.

[29] P. M. Osterberg "Electrostatically Actuated Microelectromechanical Test Structures for Material Property Measurement," Ph.D.dissertation, Massachusetts Institute of Technology, 1995.

[30] S. Pamidighantam, R. Puers, K. Baert, and H. A. C. Tilmans, "Pull-in voltage analysis of electrostatically actuated beam structures with fixed-fixed and fixed-free and conditions," *Journal of Micromechanics and Microengineering*, vol. 12, pp. 458–464, October 2002.

[31] K. Petersen, "Dynamic Micromechanics on Silicon: Techniques and Devices," *IEEE Transactions on Electron Devices*, vol. 25, no. 10, pp. 1241–1250, October 1978.

[32] C.-L. Tsai and A. K. Henning, "Out-of-plane microstructures using stress engineering of thin films," in *Proceedings of Microlithography and Metrology in Micromachining.*, vol. 2639 ,1995, pp. 124–132.

[33] C.-L. Tsai "Three dimensional stress engineered microstructures," Ph.D.dissertation, Thayer School of Engineering, Dartmouth College, 1997.